Materials Advances

ROYAL SOCIETY OF CHEMISTRY

PAPER

View Article Online
View Journal | View Issue

Cite this: *Mater. Adv.*, 2026, 7, 3822

Dipole-assisted nanoporous networks on surfaces

Huanjing Luo,[ab] Andrea Minoia,[c] Vipin Mishra, †[ab] Dariane Fadoras,[c] Filippo Giovanni Fabozzi, [d] Roberto Lazzaroni, [c] Stefan Hecht, [d] Kunal S. Mali *[ab] and Steven De Feyter *[ab]

Porous materials have evolved from rigid, strongly bonded inorganic materials, such as zeolites, to modular and adaptable metal–organic and covalent organic frameworks (MOFs and COFs), based on reversible intermolecular interactions. The shift towards weak and reversible interactions continues, where recent research has explored porous materials based on even weaker interactions, such as hydrogen bonding and electrostatic forces. Building on this trend, here we report the formation of two-dimensional (2D) honeycomb porous supramolecular networks driven by weak, yet directional dipole–dipole interactions formed at the solution–solid interface. Scanning tunneling microscopy (STM) and molecular modeling reveal how these interactions guide self-assembly and structural stability. A comparative investigation of a structurally similar building block highlights the role of molecular design and interfacial forces in tuning these interactions. Molecular mechanics and molecular dynamics (MM and MD) simulations were conducted to understand the stabilization of experimentally observed supramolecular networks, considering the roles of molecule–substrate and molecule–solvent interactions. We further report on electric field-mediated switching behavior within these networks and their ability to host suitable guest molecules. This study highlights the increasing importance of weak intermolecular forces in the design of porous materials, paving the way for dynamic and reconfigurable nanomaterials.

Received 22nd January 2026,
Accepted 26th February 2026

DOI: 10.1039/d6ma00099a

rsc.li/materials-advances

Introduction

Nanoporous materials, which contain void spaces, have been at the forefront of material science research over the past few decades.[1] The voids present within these materials can be utilized for the selective adsorption of guest molecules and chemical transformations within nanoscopic cavities. Such porous materials have a wide range of applications, including gas[2] and energy storage,[3] separation technology,[4,5] catalysis,[6] water harvesting[7] and purification,[8] sensing,[9] and environmental remediation.[10] As a consequence, significant efforts have been focused on engineering chemically stable nanoporous materials, which are often crystalline solids with high specific surface areas and well-defined, tunable pores.[11]

Porous materials exist in a diverse range of chemical and structural forms, ranging from (inorganic) crystalline aluminosilicate zeolites[12] to metal–organic frameworks (MOFs)[13] and covalent–organic frameworks (COFs).[14] The former is considered an important class due to its well-established commercial use. The widespread adoption of aluminosilicate zeolites across various industries is partly due to their high thermal and mechanical stability, which can be ascribed to the remarkably strong silicon–oxygen bond. MOFs and COFs, on the other hand, are based on relatively weak and reversible intermolecular interactions. MOFs lie at the intersection between purely inorganic materials, such as zeolites, and purely organic ones, such as COFs. They consist of organic molecules that act as struts held together by metal ion nodes *via* coordinate bonds.[13] COFs are purely organic frameworks wherein the individual organic linkers are held together *via* reversible covalent bonds.[14]

Recent years have witnessed the emergence of porous crystalline solids based on weaker interactions, such as hydrogen-bonded (H-bonded) organic frameworks (HOFs)[15] stabilized by hydrogen bonds and the so-called non-MOFs that rely on electrostatic interactions.[16] The bond energies among the aforementioned families of porous crystalline solids vary as follows: zeolites (>80 kcal mol^{-1}) $>$ COFs (50–70 kcal mol^{-1}) $>$ MOFs (20–50 kcal mol^{-1}) $>$ HOFs (10 kcal mol^{-1}), although

[a] *Division of Molecular Imaging and Photonics, Department of Chemistry, KU Leuven, Celestijnenlaan 200F, 3001 Leuven, Belgium. E-mail: kunal.mali@kuleuven.be, steven.defeyter@kuleuven.be*
[b] *KU Leuven Institute for Micro- and Nanoscale Integration (LIMNI), KU Leuven, Celestijnenlaan 200F, 3001 Leuven, Belgium*
[c] *Laboratory for Chemistry of Novel Materials, Institute of Materials Research, University of Mons, Place du Parc 20, 7000 Mons, Belgium*
[d] *Department of Chemistry and Center for the Science of Materials Berlin, Humboldt-Universität zu Berlin, 12489 Berlin, Germany*
† Current address: Department of Chemistry, School of Advanced Sciences (SAS), Vellore Institute of Technology (VIT), Vellore-632014, Tamil Nadu, India.

one expects considerable variation within each family depending on the specific linkage and structure.

While weaker intermolecular interactions render organic frameworks less robust compared to zeolites, the shift towards these materials is driven by the high degree of reversibility, which results in high crystallinity. The modular nature of organic frameworks, coupled with the possibility of isoreticular synthesis[17–19] that allows the creation of tunable cavity sizes, makes these frameworks arguably more versatile materials than zeolites. Lastly, the weak interactions that hold organic frameworks together allow for a certain degree of structural flexibility. Such flexibility, for instance, in the case of certain MOFs, enables structural transformations in response to external stimuli, which have important implications for their applications.[20]

New on-surface synthesis strategies have evolved following the advances in bulk synthesis and engineering of organic frameworks. These strategies enable the fabrication of analogous ultrathin layers of porous materials, which can then be characterized at the molecular scale using scanning probe microscopy, particularly scanning tunneling microscopy (STM). This approach provides crucial structural information, such as domain sizes, local disorder, and defects, details often missing from ensemble-averaged X-ray-based methods commonly used for characterizing the bulk counterparts. Metal–organic coordination networks (MOCNs),[21,22] analogous to single layers of two-dimensional (2D)-MOFs, 2D covalent polymers,[23–25] analogous to single layers of 2D-COFs, and H-bonded self-assembled molecular networks (SAMNs),[26–28] analogous to 2D-HOFs, have all been fabricated on solid surfaces and characterized using molecular resolution STM imaging.

2D porous networks studied on solid surfaces can be roughly categorized into two groups: those stabilized by relatively strong (and often directional) interactions (Scheme 1a and b), and those based on weaker interactions, which may or may not be directional (Scheme 1c and d). The first group includes MOCNs, 2D polymers, and H-bonded SAMNs (Scheme 1b), while the second group encompasses porous SAMNs that are stabilized by van der Waals interactions between interdigitating alkyl chains (Scheme 1d).[29,30] Porous (supramolecular) systems based on relatively stronger interactions are mostly stabilized by covalent, hydrogen, or dative bonds, wherein organic units are linked *via* strong "single or double point" contacts (Scheme 1a). The latter class also features supramolecular cavities stabilized by dispersive interactions based on weak "multiple point" contacts (Scheme 1c). Supramolecular porous networks based on weak "single point" contacts (Scheme 1e), however, are rare since such systems are thermodynamically unstable, favoring the formation of more densely packed

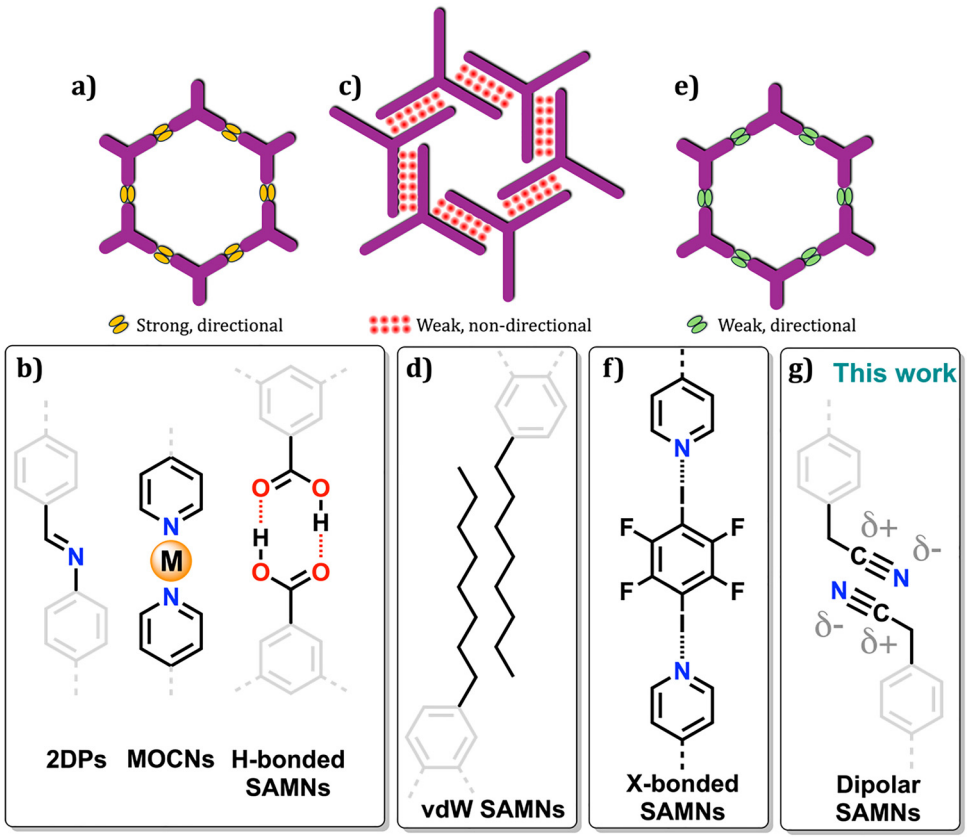

Scheme 1 An overview of porous supramolecular networks stabilized by various interactions. (a) and (b) Examples of porous networks sustained by strong and directional interactions based on a few molecular contacts. (c) and (d) Porous networks that are stabilized by weak and non-directional interactions, often based on multiple intermolecular contacts. (e)–(g) Porous networks that are stabilized by weak, yet directional interactions are rare (e) and (f). Here, we report on a porous supramolecular network assisted by dipolar interactions (g).

structures instead. A notable exception is that of halogen-bonded porous networks (Scheme 1f). These are stabilized by weak yet highly directional "single point" contacts, although only a few reports[31,32] exist on halogen-bonded porous systems at room temperature.

While several examples of H-bonded porous networks are known, to the best of our knowledge, stable low-density networks based on dipolar interactions formed at room temperature have not yet been reported. In this work, we report on a porous supramolecular network featuring weak, yet directional single-point contacts based on dipole–dipole interactions (Scheme 1g). The three-fold symmetrical molecular building block 2,2′,2″-((1,3,5-triazine-2,4,6-triyl)tris(benzene-4,1-diyl))triacetonitrile (**1**, Scheme 2a) forms a porous honeycomb network (Scheme 2b) at the alkanoic acid/graphite interface. Molecular-resolution STM images, supported by molecular mechanics and molecular dynamics (MM and MD) simulations, reveal an important contribution of molecule–substrate and molecule–solvent interactions in stabilizing the experimentally observed supramolecular networks, where dipole–dipole interactions between the peripheral nitrile groups play a structure-directing role (Scheme 2c). A comparison of the self-assembly behavior of a structurally similar building block (**2**, Scheme 2d) revealed that the triazine core and its stronger adsorption are crucial for stabilizing the honeycomb porous network. This study demonstrates how subtle variations in molecule–substrate interactions contribute to the different stabilization of the porous networks based on isostructural building blocks.

Results and discussion

Carboxylic acid groups, known for forming predictable and robust intermolecular interactions through highly directional hydrogen bonds, have been extensively used in 2D crystal engineering.[26,27,33] In contrast, nitrile groups are associated with weak hydrogen (C–H···N) or halogen (C–X···N) bonding interactions.[34,35] These interactions often compete closely with other weak interactions, making the resulting 2D (crystal) structures difficult to predict.[36] Consequently, the utility of nitrile groups in 2D crystal engineering has been somewhat limited. Despite this, the self-assembly of molecular building blocks with benzonitrile-type nodes has been extensively studied under ultra-high vacuum (UHV) conditions at low temperatures.[37] These studies primarily focused on the metal–organic coordination of the nitrile group to yield porous supramolecular networks

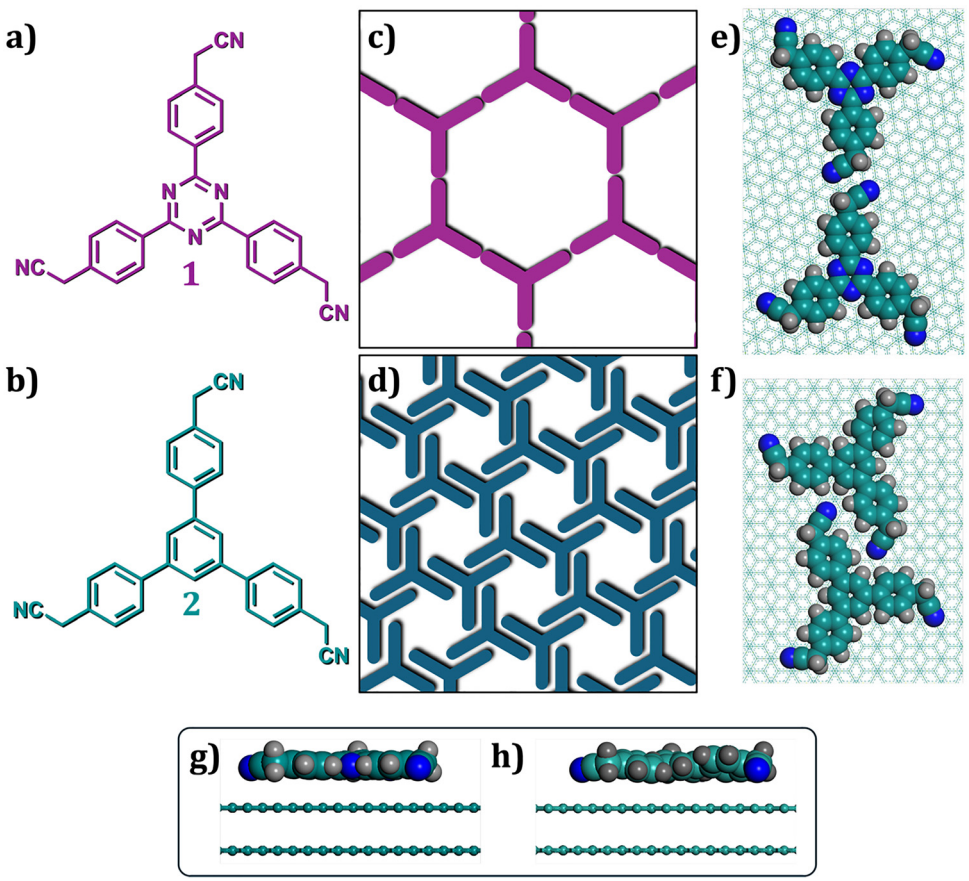

Scheme 2 (a) and (b) Molecular structures of **1** and **2**. (c) and (d) Schematics showing the type of supramolecular networks formed by **1** and **2** on graphite, respectively. (e) and (f) Supramolecular motifs that form the basis of SAMN formation in the case of **1** and **2**, respectively, on graphite. (g) and (h) MM optimized molecular structures showing the adsorption geometries of **1** and **2**, respectively, on graphite.

at low temperatures under UHV conditions.[38–42] However, studies under ambient conditions remain limited.

Alkyl-substituted cyanobiphenyls, which are liquid-crystalline materials, were among the first molecular systems to demonstrate the feasibility of performing STM imaging in liquids and were the focus of many early STM investigations.[43–46] These systems form densely packed SAMNs under ambient conditions.[47,48] With this background, we studied the self-assembly of trinitrile derivatives (Scheme 2) at the solution–solid interface. In contrast to previously studied arylnitriles, molecules **1** and **2** feature cyanomethyl groups.

Scheme 2a and b show the molecular structures of **1** and **2**, which are structurally similar and differ only in the central core. In **1**, the core is made up of a 1,3,5-triazine unit, whereas in the case of **2**, it consists of a phenyl unit. MM simulations using the PCFF force field (see SI, Section 3 for details), which incorporates ESP-derived charges, indicate that molecule 1 adopts a planar geometry in the gas phase. In contrast, molecule 2 exhibits a non-planar structure, with its cyanomethyl-substituted phenyl arms rotated approximately 34° relative to the central phenyl core (Fig. S1 in the SI). Upon adsorption on graphite, 1 remains planar, whereas the non-planarity of 2 is partially reduced (Scheme 2g and h). The dihedral angle between the phenyl arms and the central core decreases to approximately 15–20°, likely due to favorable interactions with the surface. The adsorption energy (E_{ads}) of **1** (−59.0 kcal mol^{-1}) was found to be higher than that for **2** (−56.6 kcal mol^{-1}) (Table 1). To investigate how these structural differences manifest in the on-surface assembly behavior, we studied the SAMNs of **1** and **2** at the solution–solid interface using molecular resolution STM imaging.

Fig. 1 shows the SAMN formed by **1** at the octanoic acid/graphite interface. Contrary to our expectation, molecule **1** forms relatively large domains of an ordered porous network. The domains extend over several hundred nm^2 (Fig. 1a). The high-resolution image presented in Fig. 1b clearly shows the packing arrangement of the threefold symmetric molecules of molecule **1**. The size and shape of the features in the STM images are consistent with flat-lying molecules. Each molecule occupies a lattice site in a hexagonal arrangement with its arms positioned in an end-to-end fashion to the arms of adjacent molecules in such a way that the central triazine cores and the terminal phenyl rings of adjacent molecules can be connected in an approximately straight line with a distance of ∼1.9 nm. The pore size is ∼3.0 nm (white arrow, Fig. 1b).

To gain detailed insight into the structure of the network formed by **1**, its self-assembly was modeled using MM simulations.

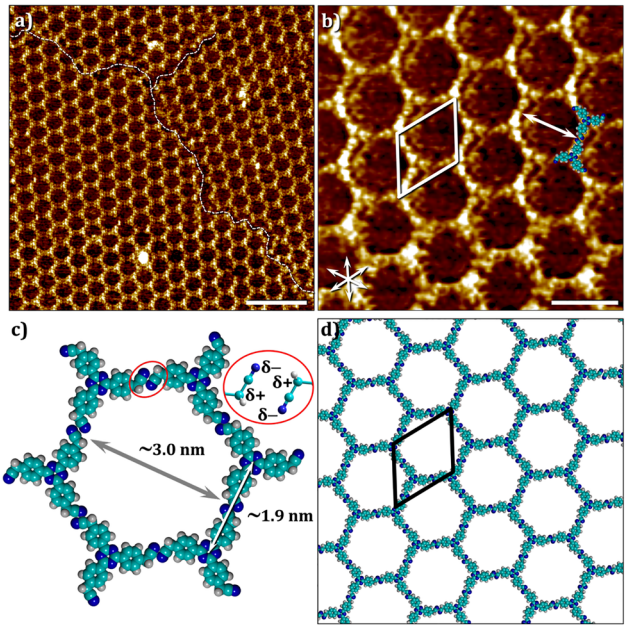

Fig. 1 (a) and (b) STM images of the SAMN formed by **1** imaged at the octanoic acid/graphite interface. [**1**] = 1.2 × 10^{-5} M. Large-scale image (a) shows the crystalline porous network formed by **1**. The dotted white line highlights domain boundaries. Scale bar = 10 nm. Imaging parameters: I_{set} = 100 pA, V_{bias} = −900 mV. High-resolution STM image (b), where the threefold symmetric molecules could be readily discerned. Unit cell parameters: a = 3.1 ± 0.2 nm, b = 3.1 ± 0.2 nm, γ = 60 ± 4°. Scale bar = 3 nm. Imaging parameters: I_{set} = 100 pA, V_{bias} = −900 mV. (c) Molecular model showing a single hexagonal motif, highlighting cavity size and intermolecular distance. Red ovals highlight the antiparallel nitrile–nitrile interactions. (d) Molecular model for the SAMN formed by **1**. For additional large-scale and high-resolution STM images, see Fig. S2 in the SI.

A hexameric unit of **1** was first constructed and its geometry optimized on a graphite surface (Fig. 1c). The resulting model closely reproduces both the experimentally observed pore size (3.0 nm) and the side length (1.8 nm) of the hexagonal network. An extended model of the self-assembled network is shown in Fig. 1d. The unit cell dimensions of this molecular model are in close agreement with those obtained from experimental STM data (see Table 1). Notably, the primary intermolecular contact revealed by the model is a dipole–dipole interaction between terminal nitrile groups arranged in an antiparallel orientation (Scheme 2e and Fig. 1c, also see Fig. S7a in the SI). The binding energy per molecule in the porous network is calculated to be −5.7 kcal mol^{-1}.

The formation of a porous network driven by dipole–dipole interactions is unexpected, considering the relatively weak

Table 1 Structural and energetic parameters of the supramolecular assemblies of **1** and **2**

	Unit cell (exp.)			Unit cell (calc.)			E_{ads} (kcal mol^{-1})	E_{int}[a] (kcal mol^{-1})	E_{bin} (kcal mol^{-1})
	a (nm)	b (nm)	γ (°)	a (nm)	b (nm)	γ (°)	Single molecule	Dimer	Network
1	3.1 ± 0.2	3.1 ± 0.2	60 ± 1	3.2	3.2	60	−59.0	−4.6	−5.7
2	2.1 ± 0.2	2.1 ± 0.2	61 ± 3	2.2	2.2	61	−56.6	−7.6	−7.0

[a] Interaction energies for experimentally observed dimer motifs.

strength of these interactions. For comparison, hydrogen bonds formed between aryl carboxylic acids, such as the dimer of benzoic acid, exhibit a bond strength of 8.6 kcal mol^{-1}.[49] In contrast, the interaction energy (E_{int}) of the dimeric motif formed by head-to-head arrangement of molecules of **1**, featuring an antiparallel arrangement of nitrile groups, was calculated to be −4.6 kcal mol^{-1} (1 **HH**, Fig. 3a and Fig. S7a in the SI). We note that the head-to-head dimer is not the most stable arrangement for **1** as well as **2**, and denser and more stable structures are possible (*vide infra*). Calculations indicate that side-by-side dense packing motifs are energetically favored over the head-to-head dimer (Fig. 3). However, the strong molecule–substrate interactions, combined with solvent-mediated stabilization (*vide infra*), promote the predominance of a head-to-head arrangement on the surface. Besides the dipole–dipole interactions, nitrile groups are also known to engage in weak hydrogen bonding interactions with aromatic C−H groups.[36] However, based on the symmetry and alignment observed in high-resolution STM images, we can rule out such hydrogen bonding in this case, as it would introduce an offset and reduce the size of the unit cell (Fig. S3 in the SI). Lastly, the dipole-stabilized SAMNs formed by **1** on graphite were found to be stable to annealing; in fact, annealed samples showed significantly higher crystallinity and domain sizes (Fig. S4 in the SI).

To evaluate whether the tendency to form stable nanoporous networks is a general feature of cyanomethyl groups, we investigated a structurally similar building block, **2**. The interaction energy of the (head-to-head) dimeric motifs formed by **2** (Fig. 3b, –4.7 kcal mol^{-1}) is comparable to that observed for **1**. However, repeated attempts to obtain STM data for this system under identical experimental conditions (*e.g.*, concentration, deposition, choice of solvent) were unsuccessful. However, at higher concentrations and with modified deposition conditions (see Experimental Section in the SI), the SAMN of molecule **2** could be observed, albeit with much reduced reproducibility. The poor experimental reproducibility observed in the case of **2** can be understood as follows. The formation of stable self-assembled networks at the solution–solid interface depends critically on both intermolecular and molecule–substrate interactions. For molecule **2**, the significantly lower adsorption energy reduces the stability and robustness of the interfacial assembly, which likely underlies its lower experimental reproducibility. This effect can be quantified through the Boltzmann factor: an adsorption energy difference of 2.4 kcal mol^{-1} implies that, under thermal equilibrium, molecule **1** is approximately 50–60 times more likely to occupy the surface than molecule **2**. Moreover, the weaker adsorption of molecule **2** makes its assemblies more susceptible to perturbation during STM imaging, where tip-induced disturbances can locally rearrange or partially disrupt weakly bound networks, further exacerbating the reduced reproducibility observed experimentally.

The large-scale STM image in Fig. 2a reveals the formation of a porous network where individual molecules are not easily discernible. The cavities within the SAMN exhibit a distinct star-shaped appearance, as shown in the inset of Fig. 2a. This unique morphology contrasts with the SAMNs of molecule **1**,

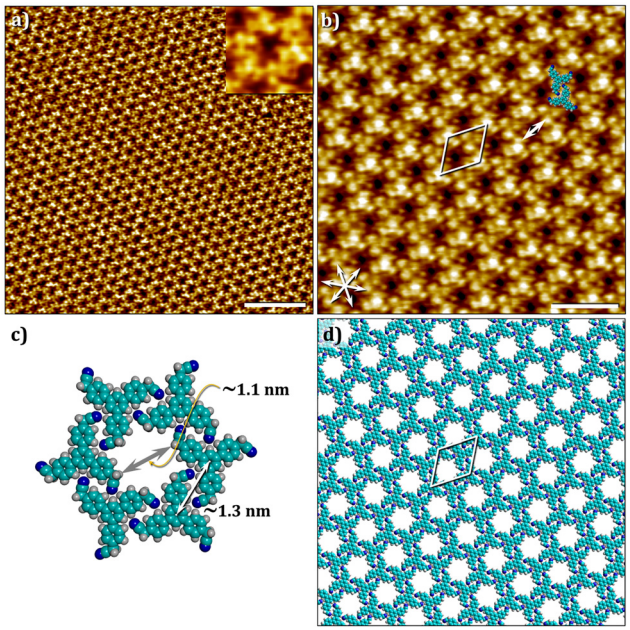

Fig. 2 (a) and (b) STM images of the SAMN formed by **2** at the octanoic acid/graphite interface [**2**] = 2.0 × 10^{-5} M. Large-scale image (a) shows the crystalline porous network formed by **2**. The inset (4 nm × 4 nm) shows the peculiar shape of the cavities within the network. Scale bar = 10 nm. Imaging parameters: I_{set} = 100 pA, V_{bias} = −1000 mV. The small-scale image (b) shows the hexagonal arrangement of molecules, wherein each molecule appears as a three- or four-lobed feature. Unit cell parameters: a = 2.1 ± 0.2 nm, b = 2.1 ± 0.2 nm, γ = 61 ± 2°. Scale bar = 5 nm Imaging parameters: I_{set} = 100 pA, V_{bias} = −1000 mV. (c) Molecular model showing a single hexagonal motif, highlighting cavity size and intermolecular distance. (d) A tentative molecular model that reproduces the symmetry and molecular arrangement observed in the high-resolution STM image presented in (b). For additional large-scale and high-resolution STM images, see Fig. S5 in the SI.

which display a smoother, circular, or hexagonal appearance (see Fig. 1a and b). The higher resolution STM image provided in Fig. 2b sheds light on the unusual shape of the cavities. In this image, individual molecules are resolved as threefold symmetric features. Each molecule appears as a group of three or four bright protrusions. We hypothesize that the periodic variation in the STM contrast of molecules (three or four-lobed) plausibly arises due to the difference in the registry of alternating molecules with respect to the graphite lattice. Most importantly, unlike **1**, molecules of **2** within the SAMN are not arranged with their arms facing each other but instead show an offset (Fig. 2b and c). Notably, molecule **1** forms the same porous network at 4 × 10^{-5} M, indicating that the denser network observed for molecule **2** is intrinsic to its assembly rather than a result of concentration-dependent polymorphism.

The interaction energy between two molecules of **2** arranged side-by-side (Fig. 3d and f), as observed in STM images, is −7.6 kcal mol^{-1}, which is higher than that of the head-to-head arrangement (Fig. 3b, *vide supra*). The pore size (∼1.1 nm) is smaller than that of the SAMN of **1**, and an offset between adjacent molecules is evident, with an intermolecular distance of ∼1.3 nm. The MM-optimized molecular model of the

hexamer of **2**, presented in Fig. 2c, corroborates with the experimentally measured pore size, intermolecular distance, and unit cell parameters. An extended optimized model of the SAMN of **2** is presented in Fig. 2d. The binding energy per molecule is calculated to be −7.0 kcal mol^{-1} (Table 1). Lastly, a hypothetical porous network based on head-to-head dimer motifs similar to those observed for molecule **1** was constructed for comparison (Fig. S7b in the SI). The binding energy per molecule in this system was found to be −4.4 kcal mol^{-1}, which is 2.6 kcal mol^{-1} lower than that of the experimentally observed network of **2**, and 1.3 kcal mol^{-1} lower than that of the experimentally observed porous network of **1** (see also Table 1).

The formation of SAMNs with ∼3.0 nm pores in the case of molecule **1** is remarkable not only because these pores are lined by molecules held together by relatively weak dipole–dipole interactions, but also because even H-bonded aromatic carboxylic acids typically begin to form alternative structures when the pore size exceeds ∼3 nm.[50] Specifically, it has been demonstrated that larger analogues of C_3-symmetric carboxylic acids do not form the regular head-to-head dimer motifs typical of these functional groups. Instead, they form dimers with a displaced geometry. These atypical dimers are stabilized by two aromatic C–H···O hydrogen bonds, rather than the two equivalent O–H···O hydrogen bonds found in the more common configuration associated with carboxyl groups.[50] This situation is similar to the SAMNs formed by molecule **2**, which also show a displaced dimer geometry and yield a smaller pore. Such shrinking of cavities can be understood by considering the thermodynamic stability of porous systems. When pores exceed a certain size, intermolecular and interfacial interactions can no longer sustain them, prompting molecular systems to adopt denser, thermodynamically favored network structures.[30,51] Since the nature of the intermolecular interactions and the size of the building blocks remain largely unchanged, it is not unreasonable to conclude that the observed difference potentially stems from differences in interfacial interactions. This interpretation is further supported by a notable 2.4 kcal mol^{-1} difference in adsorption energy (E_{ads}, single molecule) between the two building blocks (see Table 1).

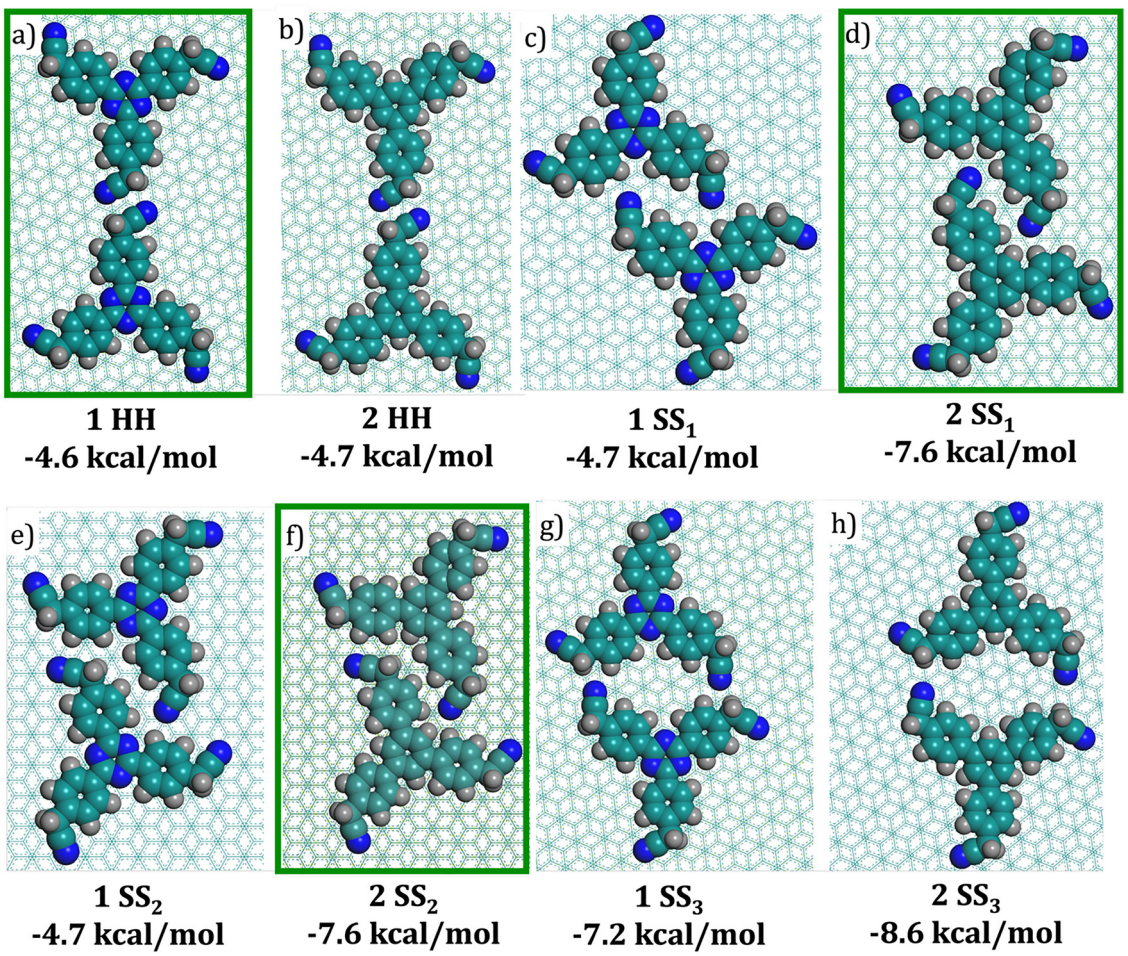

Fig. 3 An overview of the possible dimers formed by molecules **1** (a, c, e and g) and **2** (b, d, f and h), along with their interaction energies (E_{Int}), calculated using molecular mechanics (MM) calculations. **HH**: head-to-head dimers (a and b), **SS**: side-by-side dimers (c–h). The green rectangles indicate the experimentally observed networks at negative substrate bias. The other configurations may exist on the surface at positive substrate bias (see the discussion below on bias-dependent network formation).

As shown in Fig. 3, which summarizes the possible dimers formed by molecules **1** and **2** and their corresponding interaction energies, the surface dimer population of molecule **1** consists of three main dimer types (**1HH**, **1SS$_1$**, and **1SS$_2$**) with very similar interaction energies, whereas the **1SS$_3$** dimer exhibits the strongest intermolecular interaction. In contrast, molecule **2** shows a distinct interaction pattern, with strong interactions for the **2SS$_1$**, **2SS$_2$**, and **2SS$_3$** dimers and the weakest interaction for the **2HH** dimer. This analysis (Fig. 3) indicates that the dipole–dipole interactions alone are insufficient to stabilize the dimers. Furthermore, the relative strengths of the intermolecular interactions within the dimers of molecules **1** and **2** do not explain the experimentally observed formation of two distinct monolayers.

To further understand why **1** forms a dipole-assisted porous network, whereas **2** doesn't, the potential contribution of the solvent was also taken into consideration (see Section 7 in the SI for computational details). It is well established that the solvent plays a crucial role in stabilizing porous networks formed at the solution–solid interface. Alkanoic acids are known to stabilize porous SAMNs formed by aromatic tricarboxylic acids.[52] Besides dynamic co-adsorption within the cavities, MM simulations indicate that the carboxyl groups of the solvent can also engage in hydrogen bonding (E_{HB} = −3.7 kcal mol^{-1}) with the nitrile groups of **1** (Fig. S11a in the SI) as well as **2**. Furthermore, the dipole-assisted head-to-head dimer of **1** is potentially stabilized by two molecules of H-bonded solvent (Fig. S11b in the SI). Molecular models incorporating these H-bonded solvent molecules within the network exhibit identical unit cell parameters (Fig. S12 in the SI), supporting the feasibility of their stabilizing role. MD simulations (NVT, 200 ps at 300 K) show that the relatively weak hydrogen bonds between heptanoic acid and molecule **1** help preserve the head-to-head orientation. Although similar hydrogen-bonding interactions with solvent molecules are possible for molecule **2**, the MD simulations indicate that these interactions are insufficient to maintain the dipole-assisted head-to-head dimer configuration. Under the same conditions, molecule **2** instead preferentially adopts the experimentally observed side-to-side arrangement (Fig. S13 in the SI).

We emphasize that the proposed role of the solvent should be regarded as a hypothesis, as STM images do not provide conclusive evidence for the stable co-adsorption of solvent molecules within the network cavities. Nonetheless, surface-confined nanoporous networks are commonly understood to gain stabilization from dynamically adsorbed solvent molecules that undergo rapid adsorption–desorption processes on timescales much shorter than that of STM scanning. Although no solvent desorption was observed within the 200 ps molecular dynamics trajectories, we hypothesize that dynamic co-adsorption occurs at larger temporal and spatial scales. At room temperature, thermal energy is expected to facilitate solvent exchange at the interface over timescales exceeding the present computational window.

Given the recently reported electric field responsiveness of nitrile group-containing supramolecular networks[53] and the well-documented switching behavior of three-fold symmetric aromatic carboxylic acids under an electric field,[54–56] we investigated whether these two systems also respond to changes in applied sample bias. Fig. 4a shows the change in SAMN of **1** upon switching the substrate bias from negative to positive.

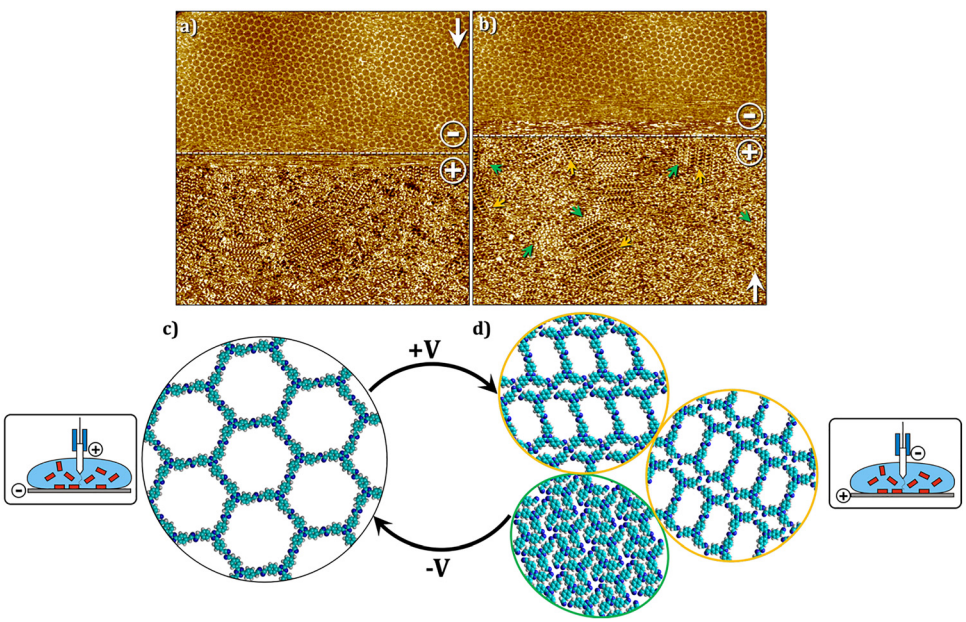

Fig. 4 (a) and (b) Representative STM images showing bias-induced structural transformation within SAMNs formed by **1**. [**1**] = 1.2 × 10^{-5} M. The STM image presented in (a) was obtained while scanning from top to bottom, and the substrate bias was changed from −700 mV to +700 mV approximately at the white dashed line. The STM image in (b) shows the opposite transition, wherein starting from the denser packing, it was possible to switch to the porous SAMN upon changing the bias from +700 mV to −700 mV. (c) and (d) Molecular models showing the main network structures involved in the bias-induced phase transition in SAMNs of **1**. +V, −V refer to the substrate bias. Imaging parameters: I_{set} = 100 pA, V_{bias} = ±700 mV.

The porous network collapses into a denser packing of molecules almost instantaneously upon the bias switch. Furthermore, the reverse structural switch can be readily achieved when the bias is switched back to negative (Fig. 4b). Cycling through the denser and porous molecular packing is possible (Fig. S14 and S15 in the SI).

While the porous network is the only structure observed at negative bias (Fig. 4c), at positive bias, several different short-range ordered domains are formed (Fig. 4d). The molecular packing within these domains exhibits two distinct arrangements, comprising a combination of side-by-side and head-to-head packings, as highlighted by the orange circles in Fig. 4d. MM simulations indicate that the most stable arrangement at the dimer level consists of one of such side-by-side configurations with an interaction energy of -7.2 kcal mol^{-1} (**1SS$_3$**, SI Fig. S8 and S9). It is notable that even for these relatively denser networks that exist under positive substrate bias, the observed intermolecular contacts often consist of the cyanomethyl dipoles, emphasizing their structure-directing role in the case of the SAMNs formed by molecule **1**.

Consistent with the difficulty of observing SAMNs of **2** using STM at the solution–solid interface, studying the bias dependence of supramolecular structures was also challenging. We were unable to observe a smooth transition from porous to denser structures within the same STM scan. Nevertheless, it was possible to establish a similar bias dependence from different experimental sessions where imaging of the monolayers was indeed possible. Fig. S16, provided in the SI, reveals that a densely packed network is exclusively observed under positive substrate bias, in contrast to the porous network displayed in Fig. 2, which is formed under negative substrate bias. Notably, this compact network lacks cyanomethyl head-to-head contacts and appears to be driven purely by close packing considerations. When the deposition and the subsequent imaging were carried out at positive bias, corresponding compact networks were observed for both molecules **1** and **2**.

The mechanism behind such bias-induced switching within physisorbed SAMNs remains under intense scrutiny. Depending on the molecular system under investigation, different hypotheses have been put forward, including conformation-dependent charge transfer processes,[54] chemical changes within adsorbed molecules,[57] and the response of polar/charged functional groups to the changes in the electric field.[53,58,59] A recent report[53] from one of us hypothesized that, in nitrile group-containing molecules, voltage-gated switching could be explained by the in-plane and out-of-plane motion of the polar nitrile groups in response to changes in the direction of the applied electric field. This hypothesis can also be used in the present case, where the 'collapse' of dipole-assisted supramolecular networks may result from the destabilization of the porous structure due to disruptions in dipole–dipole interactions, which in turn are caused by the out-of-plane orientation of the nitrile groups at positive substrate bias. Reversing the electric field direction realigns the nitrile groups in-plane, restoring the ability of the molecules to form stable porous supramolecular networks. The transition across entire molecular domains, despite the highly localized nature of the electric field ($\sim 10^9$ V m^{-1}) at the STM tip, likely arises from the scanning action effectively 'sweeping' this high-field zone across the surface. It is plausible that the phase change is initially nucleated at the tip and subsequently propagates through the domain *via* cooperative interactions or domain wall motion, remaining kinetically trapped even after the STM tip has moved away. It should be noted, however, that the dual role of the electric field, being necessary for both the induction and the observation of this phase change, presents an inherent experimental complexity in decoupling the stimulus from the measurement.

Lastly, we investigated whether the porous networks of molecule **1** could immobilize guest species, using coronene as a guest molecule. Fig. 5a and b shows STM images of the SAMN of **1** after adding a coronene solution to the preformed self-assembled network of **1**. The bright appearance of the cavities indicates the presence of coronene molecules within the host network. Individual coronene molecules could not be resolved. Given the large pore size relative to the size of the guest, we hypothesize that more than one coronene molecule is adsorbed within each pore (Fig. 5c and d) and that the cluster of coronene molecules is mobile on the time scale of STM imaging. The unit cell parameters of the host–guest network were found to be identical to those of the host network alone, indicating that guest adsorption does not alter the host network.

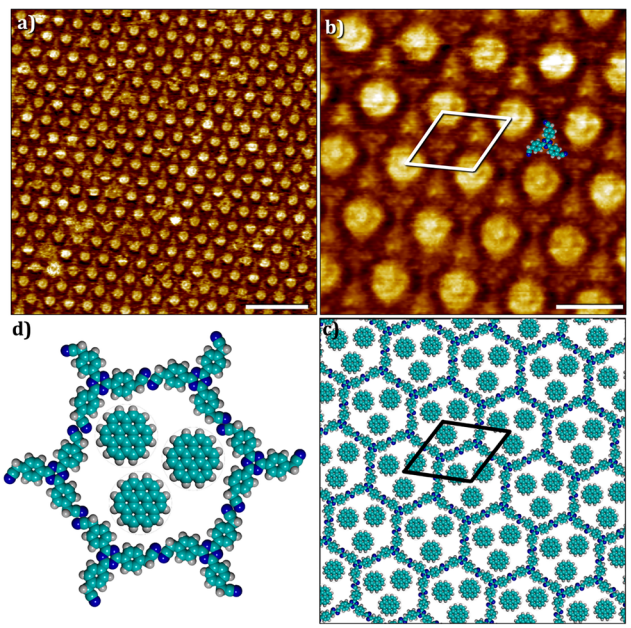

Fig. 5 (a) and (b) Large- and small-scale STM images of SAMNs of **1** with trapped coronene molecules. Individual coronene molecules were not resolved, possibly due to their in-plane mobility on the timescale of the STM measurements. Unit cell parameters: a = 3.1 ± 0.1 nm, b = 3.1 ± 0.1 nm, γ = 60 ± 2°. Imaging parameters (a), (b) I_{set} = 100 pA, V_{bias} = −700 mV. (c) A molecular model built using the experimental lattice parameters. Note that coronene molecules are presented as immobilized in an ordered fashion in the model for the sake of simplicity, whereas in reality, they are mobile within the 2D cavity and hence the fuzzy contrast in the STM image. (d) Molecular model of a single hexagonal pore showing coronene molecules. For additional STM data, see Fig. S17 in the SI.

Conclusions and outlook

The design of porous materials is increasingly shifting toward architectures based on weak intermolecular forces, enabling greater modularity and better control over crystallinity. The results described above demonstrate the formation of honeycomb porous networks assisted by dipole–dipole interactions at the solution–solid interface. High-resolution STM imaging reveals that a building block with a triazine core forms a porous honeycomb network, where the intermolecular contacts consist of nitrile dipoles. In contrast, a structurally similar building block with a phenyl core yields a hexagonal porous network with significantly smaller cavities, lacking nitrile-based dipolar contacts. A comparison of these two systems using stabilization energies obtained from molecular mechanics simulations shows that the adsorption energy of the molecular building block plays a decisive role in stabilizing the dipole-directed network. Furthermore, we demonstrated electric field-mediated switching behavior within these networks, attributed to the electric field responsiveness of the nitrile groups. Finally, the porosity of the system allows for the hosting of proper guest molecules without altering the host structure. These findings underscore the potential of weak intermolecular forces in designing dynamic and reconfigurable porous materials.

Looking ahead, there is growing interest in dynamic, reconfigurable porous architectures built on weak intermolecular forces rather than rigid covalent frameworks. By harnessing interactions such as dipole–dipole forces, it becomes possible to achieve precise, on-demand control over pore size, shape, and binding affinity. Applying external electric fields adds another layer of tunability, enabling these networks to respond in real time and transforming them from passive scaffolds into active, adaptive systems. The cyanomethyl–triazine system illustrates this shift, from constructing static materials to programming responsive ones.

Author contributions

S. D. F. and K. S. M. conceived the idea and supervised the overall work. H. L. carried out STM experiments and analyzed the STM data with the help of V. M. and F. G. F. synthesized, purified, and characterized molecules **1** and **2**. He also obtained the STM data for molecule **2**. S. H. supervised the synthesis work. A. M. and D. F. carried out MM simulations under the supervision of R. L. and K. S. M. wrote the first draft. All co-authors contributed to the subsequent revisions of the draft.

Conflicts of interest

There are no conflicts to declare.

Data availability

STM data for this article are available at KU Leuven research data repository. See DOI: https://doi.org/10.48804/GDNRHH.

Supplementary information available: experimental details (STM sample preparation, STM imaging), details of computational analysis, additional and supporting STM data, MM optimized molecular models. See DOI: https://doi.org/10.1039/d6ma00099a.

Acknowledgements

Financial support from the Research Foundation – Flanders (FWO) (G0A5U24N) and KU Leuven – Internal Funds (C14/19/079 and C14/23/090) is acknowledged. This work was in part supported by FWO (Research Foundation – Flanders (FWO)) and F.R.S. – FNRS under the Excellence of Science EOS program (projects 30489208 and 40007495). European Union's Horizon 2020 research and innovation programme under the Marie Skłodowska-Curie grant agreement No 101154831(RAPID-AFM). The molecular modeling activities in Mons are supported by FNRS and the Walloon Region (Consortium des Équipements de Calcul Intensif – CÉCI, grants U.G011.22 and 2310121). S. H. is indebted to the Einstein Foundation Berlin (EP-2021-685) as well as Humboldt University for generous support. We thank Dr. Laurens Bourda for his help in searching the Cambridge Structural Database.

Notes and references

1 T. D. Bennett, F.-X. Coudert, S. L. James and A. I. Cooper, The changing state of porous materials, *Nat. Mater.*, 2021, **20**, 1179–1187.
2 R. E. Morris and P. S. Wheatley, Gas storage in nanoporous materials, *Angew. Chem., Int. Ed.*, 2008, **47**, 4966–4981.
3 Y. Li, Z.-Y. Fu and B.-L. Su, Hierarchically structured porous materials for energy conversion and storage, *Adv. Funct. Mater.*, 2012, **22**, 4634–4667.
4 Y. Wu and B. M. Weckhuysen, Separation and purification of hydrocarbons with porous materials, *Angew. Chem., Int. Ed.*, 2021, **60**, 18930–18949.
5 R. L. Siegelman, E. J. Kim and J. R. Long, Porous materials for carbon dioxide separations, *Nat. Mater.*, 2021, **20**, 1060–1072.
6 C. Perego and R. Millini, Porous materials in catalysis: challenges for mesoporous materials, *Chem. Soc. Rev.*, 2013, **42**, 3956–3976.
7 S. Zhang, J. Fu, G. Xing, W. Zhu and T. Ben, Porous materials for atmospheric water harvesting, *ChemistryOpen*, 2023, **12**, e202300046.
8 Y. Song, J. Phipps, C. Zhu and S. Ma, Porous materials for water purification, *Angew. Chem., Int. Ed.*, 2023, **62**, e202216724.
9 L. E. Kreno, K. Leong, O. K. Farha, M. Allendorf, R. P. Van Duyne and J. T. Hupp, Metal–organic framework materials as chemical sensors, *Chem. Rev.*, 2012, **112**, 1105–1125.
10 R. Freund, O. Zaremba, G. Arnauts, R. Ameloot, G. Skorupskii, M. Dincă, A. Bavykina, J. Gascon, A. Ejsmont, J. Goscianska, M. Kalmutzki, U. Lächelt, E. Ploetz, C. S. Diercks and S. Wuttke, The current status

of MOF and COF applications, *Angew. Chem., Int. Ed.*, 2021, **60**, 23975–24001.
11 A. G. Slater and A. I. Cooper, Function-led design of new porous materials, *Science*, 2015, **348**, aaa8075.
12 M. E. Davis, Ordered porous materials for emerging applications, *Nature*, 2002, **417**, 813–821.
13 H.-C. Zhou, J. R. Long and O. M. Yaghi, Introduction to metal–organic frameworks, *Chem. Rev.*, 2012, **112**, 673–674.
14 K. T. Tan, S. Ghosh, Z. Wang, F. Wen, D. Rodríguez-San-Miguel, J. Feng, N. Huang, W. Wang, F. Zamora, X. Feng, A. Thomas and D. Jiang, Covalent organic frameworks, *Nat. Rev. Methods Primers.*, 2023, **3**, 1.
15 P. Li, M. R. Ryder and J. F. Stoddart, Hydrogen-bonded organic frameworks: A rising class of porous molecular materials, *Acc. Mater. Res.*, 2020, **1**, 77–87.
16 M. O'Shaughnessy, J. Glover, R. Hafizi, M. Barhi, R. Clowes, S. Y. Chong, S. P. Argent, G. M. Day and A. I. Cooper, Porous isoreticular non-metal organic frameworks, *Nature*, 2024, **630**, 102–108.
17 Z. Mai and D. Liu, Synthesis and applications of isoreticular metal–organic frameworks IRMOFs-*n* (*n* = 1, 3, 6, 8), *Cryst. Growth Des.*, 2019, **19**, 7439–7462.
18 R. Freund, S. Canossa, S. M. Cohen, W. Yan, H. Deng, V. Guillerm, M. Eddaoudi, D. G. Madden, D. Fairen-Jimenez, H. Lyu, L. K. Macreadie, Z. Ji, Y. Zhang, B. Wang, F. Haase, C. Wöll, O. Zaremba, J. Andreo, S. Wuttke and C. S. Diercks, 25 years of reticular chemistry, *Angew. Chem., Int. Ed.*, 2021, **60**, 23946–23974.
19 O. M. Yaghi, Reticular chemistry in all dimensions, *ACS Cent. Sci.*, 2019, **5**, 1295–1300.
20 A. Schneemann, V. Bon, I. Schwedler, I. Senkovska, S. Kaskel and R. A. Fischer, Flexible metal–organic frameworks, *Chem. Soc. Rev.*, 2014, **43**, 6062–6096.
21 J. V. Barth, G. Costantini and K. Kern, Engineering atomic and molecular nanostructures at surfaces, *Nature*, 2005, **437**, 671–679.
22 J. Liu, M. Abel and N. Lin, On-surface synthesis: a new route realizing single-layer conjugated metal–organic structures, *J. Phys. Chem. Lett.*, 2022, **13**, 1356–1365.
23 M. Lackinger, On-surface polymerization – a versatile synthetic route to two-dimensional polymers, *Polym. Int.*, 2015, **64**, 1073–1078.
24 A. M. Evans, M. J. Strauss, A. R. Corcos, Z. Hirani, W. Ji, L. S. Hamachi, X. Aguilar-Enriquez, A. D. Chavez, B. J. Smith and W. R. Dichtel, Two-dimensional polymers and polymerizations, *Chem. Rev.*, 2022, **122**, 442–564.
25 Z.-F. Cai, T. Chen and D. Wang, Insights into the polymerization reactions on solid surfaces provided by scanning tunneling microscopy, *J. Phys. Chem. Lett.*, 2023, **14**, 2463–2472.
26 A. G. Slater, P. H. Beton and N. R. Champness, Two-dimensional supramolecular chemistry on surfaces, *Chem. Sci.*, 2011, **2**, 1440–1448.
27 M. Lackinger and W. M. Heckl, Carboxylic acids: versatile building blocks and mediators for two-dimensional supramolecular self-assembly, *Langmuir*, 2009, **25**, 11307–11321.
28 M. O. Blunt, J. C. Russell, M. D. C. Gimenez-Lopez, N. Taleb, X. Lin, M. Schröder, N. R. Champness and P. H. Beton, Guest-induced growth of a surface-based supramolecular bilayer, *Nat. Chem.*, 2011, **3**, 74–78.
29 K. Tahara, S. Lei, J. Adisoejoso, S. De Feyter and Y. Tobe, Supramolecular surface-confined architectures created by self-assembly of triangular phenylene-ethynylene macrocycles via van der Waals interaction, *Chem. Commun.*, 2010, **46**, 8507–8525.
30 X. Shen, X. Wei, P. Tan, Y. Yu, B. Yang, Z. Gong, H. Zhang, H. Lin, Y. Li, Q. Li, Y. Xie and L. Chi, Concentration-controlled reversible phase transitions in self-assembled monolayers on HOPG surfaces, *Small*, 2015, **11**, 2284–2290.
31 A. Mukherjee, J. Teyssandier, G. Hennrich, S. De Feyter and K. S. Mali, Two-dimensional crystal engineering using halogen and hydrogen bonds: towards structural landscapes, *Chem. Sci.*, 2017, **8**, 3759–3769.
32 Q.-N. Zheng, X.-H. Liu, T. Chen, H.-J. Yan, T. Cook, D. Wang, P. J. Stang and L.-J. Wan, Formation of halogen bond-based 2D supramolecular assemblies by electric manipulation, *J. Am. Chem. Soc.*, 2015, **137**, 6128–6131.
33 O. Ivasenko and D. F. Perepichka, Mastering fundamentals of supramolecular design with carboxylic acids. Common lessons from X-ray crystallography and scanning tunneling microscopy, *Chem. Soc. Rev.*, 2011, **40**, 191–206.
34 N. Wintjes, J. Hornung, J. Lobo-Checa, T. Voigt, T. Samuely, C. Thilgen, M. Stöhr, F. Diederich and T. A. Jung, Supramolecular synthons on surfaces: controlling dimensionality and periodicity of tetraarylporphyrin assemblies by the interplay of cyano and alkoxy substituents, *Chem. – Eur. J.*, 2008, **14**, 5794–5802.
35 K. S. Ingle, K. M. Bairagi, J. S. Thakur, R. Sathishkumar, R. Chennuru, B. Baishya and S. K. Nayak, Synthesis, structural and theoretical analyses of C≡N···I halogen-bonded liquid crystalline complexes of 4-cyano-4′-alkoxy biphenyl systems, *Cryst. Growth Des.*, 2023, **23**, 1755–1767.
36 K. E. Maly, T. Maris, E. Gagnon and J. D. Wuest, Inclusion compounds of hexakis(4-cyanophenyl)benzene: open networks maintained by C–H···N interactions, *Cryst. Growth Des.*, 2006, **6**, 461–466.
37 S. Klyatskaya, F. Klappenberger, U. Schlickum, D. Kühne, M. Marschall, J. Reichert, R. Decker, W. Krenner, G. Zoppellaro, H. Brune, J. V. Barth and M. Ruben, Surface-confined self-assembly of di-carbonitrile polyphenyls, *Adv. Funct. Mater.*, 2011, **21**, 1230–1240.
38 U. Schlickum, R. Decker, F. Klappenberger, G. Zoppellaro, S. Klyatskaya, M. Ruben, I. Silanes, A. Arnau, K. Kern, H. Brune and J. V. Barth, Metal–organic honeycomb nanomeshes with tunable cavity size, *Nano Lett.*, 2007, **7**, 3813–3817.
39 D. Kühne, F. Klappenberger, R. Decker, U. Schlickum, H. Brune, S. Klyatskaya, M. Ruben and J. V. Barth, High-quality 2D metal–organic coordination network providing giant cavities within mesoscale domains, *J. Am. Chem. Soc.*, 2009, **131**, 3881–3883.

40 J. I. Urgel, D. Écija, G. Lyu, R. Zhang, C.-A. Palma, W. Auwärter, N. Lin and J. V. Barth, Quasicrystallinity expressed in two-dimensional coordination networks, *Nat. Chem.*, 2016, **8**, 657–662.

41 S. Gottardi, K. Müller, J. C. Moreno-López, H. Yildirim, U. Meinhardt, M. Kivala, A. Kara and M. Stöhr, Cyano-functionalized triarylamines on Au(111): competing intermolecular versus molecule/substrate interactions, *Adv. Mater. Interfaces*, 2014, **1**, 1300025.

42 K. Müller, J. C. Moreno-López, S. Gottardi, U. Meinhardt, H. Yildirim, A. Kara, M. Kivala and M. Stöhr, Cyano-functionalized triarylamines on coinage metal surfaces: interplay of intermolecular and molecule–substrate interactions, *Chem. – Eur. J.*, 2016, **22**, 581–589.

43 D. P. E. Smith, J. K. H. Hörber, G. Binnig and H. Nejoh, Structure, registry and imaging mechanism of alkylcyanobiphenyl molecules by tunnelling microscopy, *Nature*, 1990, **344**, 641–644.

44 J. S. Foster and J. E. Frommer, Imaging of liquid crystals using a tunnelling microscope, *Nature*, 1988, **333**, 542–545.

45 D. P. E. Smith, H. Hörber, C. Gerber and G. Binnig, Smectic liquid crystal monolayers on graphite observed by scanning tunneling microscopy, *Science*, 1989, **245**, 43–45.

46 M. Hara, Y. Iwakabe, K. Tochigi, H. Sasabe, A. F. Garito and A. Yamada, Anchoring structure of smectic liquid-crystal layers on MoS_2 observed by scanning tunnelling microscopy, *Nature*, 1990, **344**, 228–230.

47 S. Snegir, Y. J. Dappe, O. L. Kapitanchuk, D. Coursault and E. Lacaze, Kinked row-induced chirality driven by molecule–substrate interactions, *Phys. Chem. Chem. Phys.*, 2020, **22**, 7259–7267.

48 H. D. Castillo, J. M. Espinosa-Duran, J. R. Dobscha, D. C. Ashley, S. Debnath, B. E. Hirsch, S. R. Schrecke, M.-H. Baik, P. J. Ortoleva, K. Raghavachari, A. H. Flood and S. L. Tait, Amphiphile self-assembly dynamics at the solution–solid interface reveal asymmetry in head/tail desorption, *Chem. Commun.*, 2018, **54**, 10076–10079.

49 P. Novak, D. Vikić-Topić, Z. Meić, S. Sekušak and A. Sabljić, Investigation of hydrogen bond structure in benzoic acid solutions, *J. Mol. Struct.*, 1995, **356**, 131–141.

50 J. F. Dienstmaier, K. Mahata, H. Walch, W. M. Heckl, M. Schmittel and M. Lackinger, On the scalability of supramolecular networks – high packing density *vs.* optimized hydrogen bonds in tricarboxylic acid monolayers, *Langmuir*, 2010, **26**, 10708–10716.

51 S. Lei, K. Tahara, F. C. De Schryver, M. Van der Auweraer, Y. Tobe and S. De Feyter, One building block, two different supramolecular surface-confined patterns: concentration in control at the solid–liquid interface, *Angew. Chem., Int. Ed.*, 2008, **47**, 2964–2968.

52 O. Ochs, M. Hocke, S. Spitzer, W. M. Heckl, N. Martsinovich and M. Lackinger, Origin of solvent-induced polymorphism in self-assembly of trimesic acid monolayers at solid–liquid interfaces, *Chem. Mater.*, 2020, **32**(12), 5057–5065.

53 F. G. Fabozzi, J. D. Cojal González, N. Severin, J. P. Rabe and S. Hecht, Voltage-gated switching of moiré patterns in epitaxial molecular crystals, *ACS Nano*, 2024, **18**, 33664–33670.

54 F. P. Cometto, K. Kern and M. Lingenfelder, Local conformational switching of supramolecular networks at the solid/liquid interface, *ACS Nano*, 2015, **9**, 5544–5550.

55 S.-L. Lee, Y. Fang, G. Velpula, F. P. Cometto, M. Lingenfelder, K. Müllen, K. S. Mali and S. De Feyter, Reversible local and global switching in multicomponent supramolecular networks: controlled guest release and capture at the solution/solid interface, *ACS Nano*, 2015, **9**, 11608–11617.

56 A. Mahmood, X. Zeng, A. S. Saleemi, K.-Y. Cheng and S.-L. Lee, Electric-field-induced supramolecular phase transitions at the liquid/solid interface: cat-assembly from solvent additives, *Chem. Commun.*, 2020, **56**, 8790–8793.

57 G. Velpula, J. Teyssandier, S. De Feyter and K. S. Mali, Nanoscale control over the mixing behavior of surface-confined bicomponent supramolecular networks using an oriented external electric field, *ACS Nano*, 2017, **11**, 10903–10913.

58 S.-B. Lei, K. Deng, Y.-L. Yang, Q.-D. Zeng, C. Wang and J.-Z. Jiang, Electric driven molecular switching of asymmetric tris(phthalocyaninato) lutetium triple-decker complex at the liquid/solid interface, *Nano Lett.*, 2008, **8**, 1836–1843.

59 K. S. Mali, D. Wu, X. Feng, K. Müllen, M. Van der Auweraer and S. De Feyter, Scanning tunneling microscopy-induced reversible phase transformation in the two-dimensional crystal of a positively charged discotic polycyclic aromatic hydrocarbon, *J. Am. Chem. Soc.*, 2011, **133**, 5686–5688.